Harnessing Mechanical Deformation to Reduce Spherical Aberration in Soft Lenses

Ahmad Zareei,[†] Eder Medina,[†] and Katia Bertoldi[*]

School of Engineering and Applied Sciences, Harvard University, Cambridge, Massachusetts 02148, USA

Mechanical deformation has recently emerged as a promising platform to realize optical devices with tunable response. While most studies to date have focused on the tuning of the focal length, here we use a combination of experiments and analyses to show that an applied tensile strain can also largely reduce spherical aberration. We first demonstrate the concept for a cylindrical elastomeric lens and then show that it is robust and valid over a range of geometries and material properties. As such, our study suggests that large mechanical deformations may provide a simple route to achieve the complex profiles required to minimize aberration and realize lenses capable of producing images of superior quality.

From programmable flexible metamaterials [1–5] and self-regulating fluidics [6,7] to smart drug delivery systems [8–11] and scaffolds for tissue engineering [12,13], soft materials have enabled the design of a wide range of functional structures with tunable response. In particular, inspired by the crystalline lens and ciliary muscle of the human eye, intense efforts have been devoted to the design of optical lenses with adjustable focus. To realize these tunable optical systems several strategies have been pursued. On the one hand, it has been shown that the focus can be tuned by varying the pressure of fluid enclosed by a lens-shaped flexible chamber [14–18]. On the other hand, fully solid lenses capable of focal adjustment have been realized by mechanically or electrically stretching soft membranes [19–27]. However, despite the fact that the quality of the images produced by the lenses is affected by many optical properties, including spherical aberration, tilt, coma, and distortion, these design strategies predominantly consider focal point adaptation [19–27] and to a limited extent other optical properties such as astigmatism [25–27] and spherical aberration [28]. In particular, though spherical aberration has been shown to reduce in thin lenses upon bending [28], the effect of other elastic deformations on this important optical property has not been explored yet.

In this Letter, we show that by pulling an elastomeric biconvex lens we not only alter its focal length, but can also largely reduce its spherical aberration. While in the undeformed configuration our elastomeric lens exhibits spherical aberration—as it fails to focus all monochromatic rays to the same point [see Fig. 1(a)]—we find that a critical applied strain exists for which aberration is largely reduced [see Fig. 1(b)]. We first use a combination of experiments and analysis to demonstrate the concept on a cylindrical lens and then show that the same strategy can also be extended to spherical lenses. As such, our results indicate that nonlinear deformations may provide an effective pathway to realize the complex surface profiles required

for aberration-free lenses starting from simple and easy to manufacture shapes.

We consider a cylindrical biconvex lens formed through the intersection of two cylinders of radius R_r and R_l and center-to-center distance Δx that are aligned along the z axis. Such a lens has a thickness $t = R_r + R_l - \Delta x$ and height $2h$, as it is truncated by two xz planes located at a distance h from the symmetry plane [see Fig. 1(c)]. Further, it is made of an elastomeric material and is stretched by applying a y displacement v to its top nonrefracting boundary (while fixing the bottom one). We first conduct finite element (FE) analyses within the open-source library Firedrake [29] to investigate the deformation of such soft lenses. We assume plain strain conditions and use higher order quadratic boundary conforming elements to mitigate
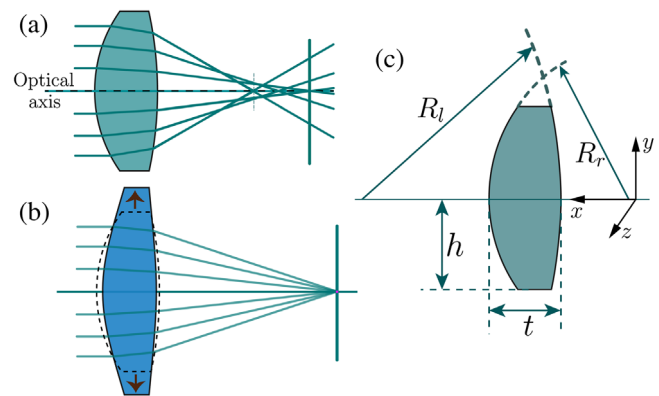

FIG. 1. Harnessing mechanical deformation to reduce spherical aberration in soft lenses. (a),(b) Schematic of a soft lens (a) in its undeformed and (b) stretched configuration. When the lens is at rest, it exhibits spherical aberration as the rays do not converge to a single point. In the stretched configuration not only the focal length increases but also the spherical aberration may be largely reduced. (c) Schematic of the cylindrical biconvex lens considered in this study.

mesh discretization errors of the surfaces. Moreover, we capture the material response with a compressible neo-Hookean model with strain energy density Ψ given by

$$\Psi = \frac{\mu}{2}[\text{tr}(\mathbf{F}^\top \mathbf{F}) - 3] - \mu \det(\mathbf{F}) + \frac{\mu\nu}{1 - 2\nu}\log(\det \mathbf{F})^2, \quad (1)$$

where $\mathbf{F}$ is the deformation gradient, μ is the shear modulus, and ν is the Poisson ratio (see Supplemental Material for details). For each given deformed configuration, we then use geometrical ray tracing [30] to compute the trajectories of incident rays that travel parallel to the optical axis (i.e., parallel to the x axis). Note that, while the refractive index n generally varies with the material stress [31], for the material and range of applied deformation considered in here such changes are negligible [i.e., $\max(\Delta n) \approx 0.1\%$]. As such, in our calculations we assume n to be constant.

In Fig. 2(a) we show the deformed configurations as well as the computed ray trajectories for a lens with $R_r/h = 1.6$, $R_l/h = 60$, $t/h = 0.72$, $\nu = 0.45$, and $n = 1.4$ at $\varepsilon = v/2h = 0$ (i.e., undeformed configuration) and 10.6%. Our results indicate that, while rays entering the lens near the optical axis converge at the paraxial focal point F (located at a distance f from the right surface), those that reach the lens at $y \gg 0$ intersect the optical axis at a distance $\ell(y)$ from F. For $\varepsilon = 0$, we find that $f = 3.41h$ and $\ell(y)/h \sim 0.28(y/h)^2$. Differently, for $\varepsilon = 10.6\%$ the paraxial focal point distance increases to $3.82\,h$ and $\ell(y) \sim 0$. As such, these results indicate that the applied deformation not only enables us to tune the focus of the lens, but can also be exploited to reduce its aberration.

In order to better quantify the effect of the applied deformation on aberration, we introduce a longitudinal measure of the spherical aberration, $\mathcal{L} = \max \ell(y)$ for $y \in [-0.8h, 0.8h]$, where this range is chosen to avoid highly nonlinear boundary effects [32]. In Fig. 2(b) we plot the evolution of both the paraxial focal point distance f and longitudinal measure of the spherical aberration $\mathcal{L}$ as a function of the applied strain ε. The results indicate that, while f increases linearly with ε, $\mathcal{L}$ first decreases, reaches a minimum at $\varepsilon = \varepsilon_{\min} = 10.6\%$, and then further increases. To gain more insight into the physical ingredients underlying the observed phenomenon, we examine the deformed shape of the stretched lens. Toward this end, in Fig. 2(c) we report the maximum principal stretch $\lambda_{\max}$ and its directions at $\varepsilon_{\min}$. We find that the deformation is minimal in the region close to the left surface near the optical axis, so that the initial spherical curvature is preserved there. However, away from the optical axis the lens deforms nonuniformly making the surfaces deviate from their initial spherical profile—a fact that is known to promote reduction in spherical aberration [33].

Next, to validate our numerical findings, we fabricate a lens identical to that considered in Fig. 1(b) (with $t = 18$ mm) out of a transparent silicone elastomer
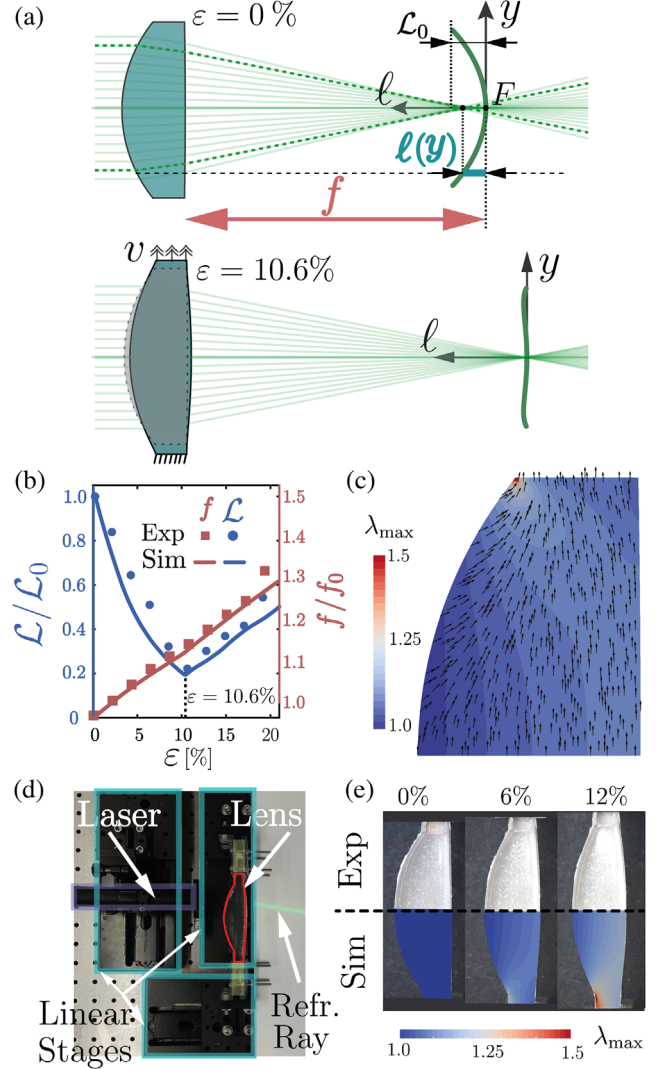

FIG. 2. Pulling of a biconvex cylindrical lens with $R_r/h = 1.6$, $R_l/h = 60$, $t/h = 0.72$. (a) Ray trajectories at $\varepsilon = 0\%$ (top) and $\varepsilon = \varepsilon_{\min} = 10.6\%$ (bottom). (b) Evolution of $\mathcal{L}/\mathcal{L}_0$ (blue) and f/f_0 (red) as a function of ε, where $\mathcal{L}_0 = \mathcal{L}(\varepsilon = 0) = 0.05h$ and $f_0 = f(\varepsilon = 0) = 5.6h$. Both experimental (markers) and numerical (solid lines) results are shown. (c) Numerically predicted magnitude and direction of the maximum principal stretch at $\varepsilon = \varepsilon_{\min} = 10.6\%$. (d) Experimental setup. (e) Experimental (top) and numerical (bottom) snapshots of the lens at different levels of applied deformation. For the numerical images, we also show the maximum principal stretch $\lambda_{\max}$ in the deformed configurations.

(Slygard 184—see Supplemental Material [34] for details). In our tests we clamp the lens at its flat boundaries and use a linear stage motor (ThorLabs-LTS300) to stretch it [see Fig. 2(c)]. At different levels of applied deformation we then scan the left surface of the lens with a laser (LT-301 500 mW) mounted on a separate linear stage and pointed parallel to lens optical axis, while recording the trajectories of the reflected ray with a camera (SonyRX400—see Supplemental Material [34] for details). We find the

experimental results nicely match both the deformed shape [Fig. 2(d)] as well as the evolution of f and $\mathcal{L}$ [Fig. 2(b)] predicted by our numerical analyses, with small discrepancies due to unavoidable imperfections introduced during fabrication and testing. As such, these results confirm that pulling a biconvex lens, in addition to increasing its focal length, also reduces the longitudinal measure of spherical aberration.

The deformation-induced reduction in longitudinal aberration observed in both experiments and simulations [Fig. 2(b)] suggests that at a critical strain the lens surface approaches the profile of a perfect zero-aberration lens. To quantify the agreement between the two geometries, we first analytically derive the surface profile for an aberration-free lens and then compare it with that of our stretched lens. To this end, we use Fermat's principle which states that incident rays emanating from the same source plane and converging at an identical point must have equal optical path lengths. In particular, we consider the optical path of an arbitrary far-field ray that enters the left lens surface point Q, exits at the right surface at point P and intersects the optical axis at the focal point at angle an angle θ. The optical path length of such ray between the yz plane passing through the leftmost point of the lens and the focal point is given by

$$\Lambda^P = n_0[f + L_0 - L(\theta) - x_P] + n\frac{L(\theta)}{\cos(\delta)}$$
$$+ n_0\sqrt{x_P^2(\theta) + y_P^2(\theta)}, \tag{2}$$

where n_0 denotes the refractive index of the surrounding medium, $L(\theta)$ represents the horizontal distance traveled through the lens, $L_0 \equiv L(\theta = 0)$ and (x_p, y_p) are the coordinates at point P. Moreover, δ is the angle between the horizontal axis and the in-lens ray path [Fig. 3(a)], which is determined by Snell's law

$$n\sin(\psi + \delta) = n_0\sin(\theta + \psi), \tag{3}$$

with $\psi = \tan^{-1}(dx_P/dy_P)$. Note that the first, second, and third terms in Eq. (2) denote the optical distances traveled by the off-axis ray to (i) arrive at point Q from the selected yz plane, (ii) traverse the lens, and (iii) reach the focal point from point P. Since for a ray traveling along the optical axis (for which $\theta = 0$ and $y_p = 0$) Eq. (2) reduces to

$$\Lambda^{\text{ax}} = nL_0 + n_0 f, \tag{4}$$

the aberration-free lens at each level of applied strain is calculated by imposing $\Lambda^P = \Lambda^{\text{ax}}$, while inputting the right surface coordinates (x_p, y_p), focal distance f, and deformed lens thickness L_0, obtained in the FE simulation [35]. In Fig. 3(b) we analyze the difference in the coordinates of the left surface of the aberration-free lens defined by $\mathbf{x}^{\text{An}} = [x_p + L(\theta)/\cos\delta, y_p + L(\theta)/\sin\delta]$ and
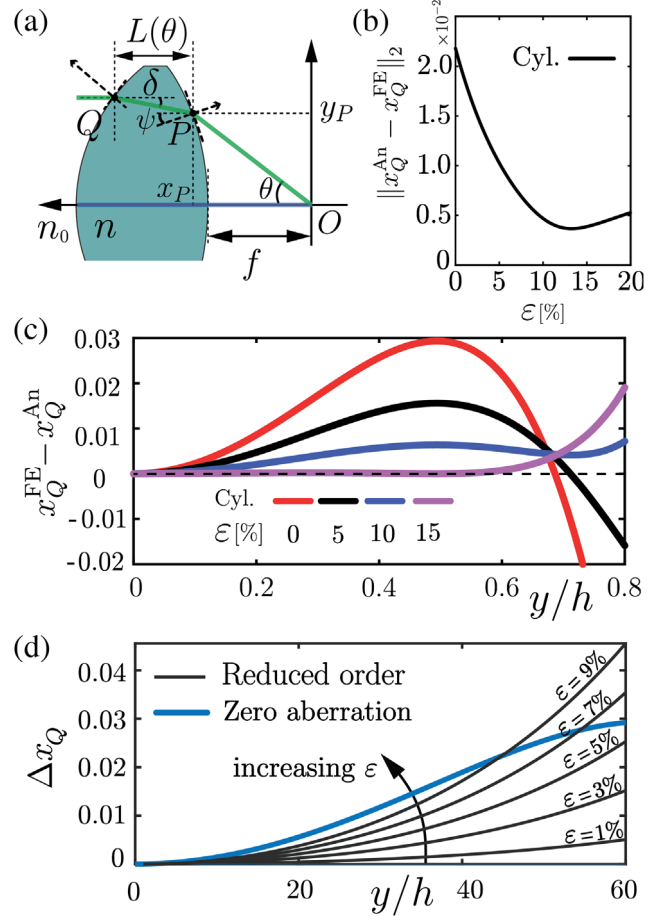

FIG. 3. Aberration-free profiles. (a) Schematic of our cylindrical biconvex lenses. (b) Evolution of L^2-norm difference between the coordinates of the left surface of the aberration-free lens and the simulated one $\|x_Q^{\text{An}} - x_Q^{\text{FE}}\|$ as a function of the applied strain ε for the lens considered in Fig. 2. (c) Difference between the stretched profile and an aberration-free profile $x_Q^{\text{FE}} - x_Q^{\text{An}}$ along the lens height y/h. (d) Left surface deviation from its initial configuration at different strains predicted by the reduced order model (black lines), and the deviation required for a zero-aberration lens surface (blue line).

the simulated coordinates $\mathbf{x}^{\text{FE}}$ by looking at their L^2-norm difference for $y \in (0, 0.8h)$ as a function of the applied strain ε. We find that the surface quickly approaches the aberration-free profile and then gradually deviates from it at larger strains, with the L^2-norm difference that reaches a nonzero minimum at ε_{min}. As such, these results indicate that the nonlinear deformation caused by applied strain ε_{min} results in a lens profile with nonconstant curvature very close to that required to remove aberration in a biconvex cylindrical lens. To further understand the effect of the applied deformation on aberration, we plot the difference between the aberration-free and stretched profiles along the lens height. The results reported in Fig. 3(c) show that different regions of the lens approach the aberration free surface at different rates. As the strain is applied the entire

lens converges toward the aberration-free profile until a small difference is reached at $\varepsilon_{\min}$. Any additional deformation then causes the region next to the boundaries to diverge while the inner region continues to converge closer to the aberration-free profile. These two contrasting trends lead to an increase of L^2-norm difference between the coordinates of the left surface of the aberration-free lens for $\varepsilon > \varepsilon_{\min}$. Therefore, our results indicate that the combined deformations of the right and left surface, and the change in the lens thickness caused by the applied deformation contribute in a complex way to the observed reduction in aberration.

Next, to further elucidate the effect of deformation on aberration reduction, we developed a reduced order model where we describe the cylindrical lens as a series of infinitesimal hyperelastic rectangular elements undergoing uniaxial deformation and assume that the right surface remains flat throughout the stretching process (see Supplemental Material [34] for details). This simple model allows us to describe the left surface profile as a function of applied strain and, therefore, quantify the effect of stretching on aberration. In Fig. 3(d) we plot the left surface deviation from its initial configuration at different strains predicted by the reduced order model (black lines), and the deviation required for a zero-aberration lens surface [defined by Eqs. (2)–(4), blue line]. In agreement with the results of our FE simulations, we find that the left surface of the lens approaches the profile of a zero-aberration lens as ε increases, but the profiles never fully coincide. As such, the reduced order model points to the robustness of the observed phenomenon, as it shows that the stretching-induced reduction in aberration can be observed as geometric parameters are varied.

Having demonstrated that the applied deformation can be exploited to largely reduce aberration in a cylindrical lens, we now show that the phenomenon persists for a wide range of geometrical and material properties and that can be also extended to spherical lenses. In Figs. 4(a)–4(d) we report the numerically predicted evolution of $\mathcal{L}$ as a function of the applied deformation for a large set of cylindrical lenses as well as spherical ones, which are deformed by radially stretching their nonrefracting boundaries (see Supplemental Material [34] for details). The results indicate that regardless of geometry and Poisson's ratio, the applied stretching can be harnessed to reduce aberration of both cylindrical and spherical biconvex lenses by ∼85%–90%. Further, by comparing the response of the spherical and cylindrical lenses, we find that the former require a smaller applied strain to minimize $\mathcal{L}$. The results of Figs. 4(a)–4(d) also show that for all sets of considered parameters the aberration curves follow a similar trajectory (i.e., decreasing to a minimum reached and increasing afterward) with the strain at which the aberration is minimum, $\varepsilon_{\min}$, determined by a complex interplay between mechanics, geometry, and optical
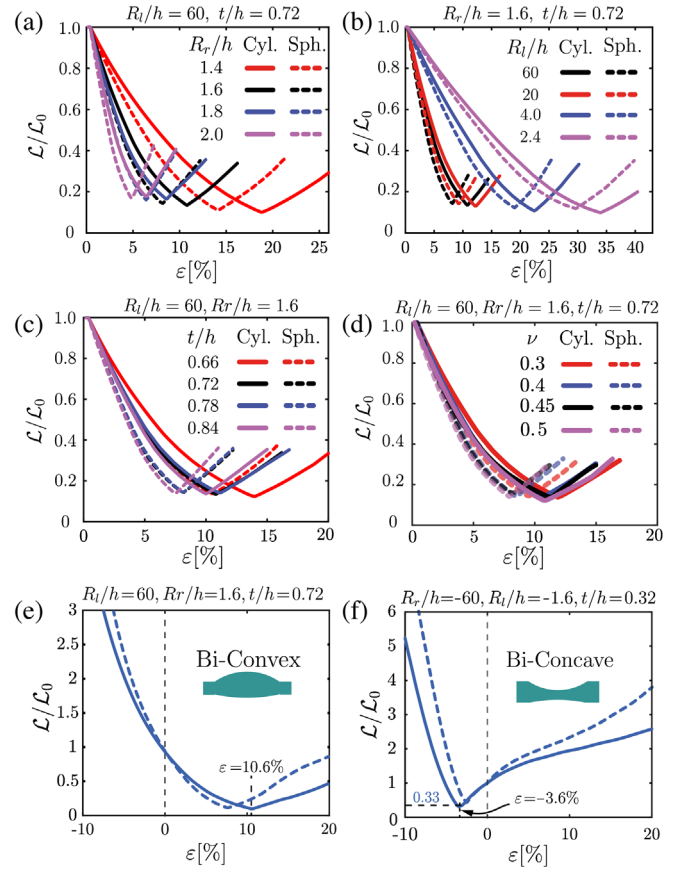

FIG. 4. Effect of geometry, material, and loading direction on $\mathcal{L}$. (a)–(e) Effect of (a) R_r/h, (b) R_l/h, (c) t/h, (d) ν (note that $\nu = 0.5$ requires an incompressible strain energy function ψ; see Supplemental Material [34] for details), and (e) loading direction on $\mathcal{L}$ for both cylindrical (solid lines) and spherical (dashed lines) biconvex lenses. (f) Effect of loading direction on $\mathcal{L}$ for a biconcave lens.

properties. The dependence of $\varepsilon_{\min}$ to various geometrical parameters can be extracted from our numerical results and can be used for the lens design (see Supplemental Material [34] for details). We would further like to point out that $\varepsilon_{\min}$ not only depends on geometrical and material parameters, but also it depends on the aperture size (i.e., the area of the lens considered). A smaller aperture results in smaller initial aberration. However, since the central region of the lens is slower in approaching the zero-aberration profile, $\varepsilon_{\min}$ becomes larger (see Fig. S4). Remarkably, the aberration reduction persists independent of geometrical and material properties and initial aperture size.

While the proposed concept is robust with respect to geometric variations, it is important to recognize that the direction of the applied deformation plays a crucial role. As shown in Fig. 4(e), differently from the pulling considered thus far, an applied compressive deformation further accentuates the initial aberration as it locally changes the lens' surfaces to move them away from the aberration-free profiles (see Fig. S3). Differently, a compression load may

reduce aberration in a biconcave lens [see Fig. 4(f) for a lens characterized by $R_r/h = -60$, $R_l/h = -1.6$, and $t/h = 0.32$], but such reduction is limited to small levels of strain as under compression a buckling instability is triggered that significantly alters its geometry (Movie S1).

To summarize, we have demonstrated that mechanical deformation can be harnessed to reduce spherical aberration of cylindrical and spherical biconvex soft lenses. More specifically, we have used analyses to show that a critical strain exists for which the profile of the deformed lens closely approaches the shape of an aberration-free one and also demonstrated the concept experimentally. Although in this study we have focused on conventional biconvex and biconcave elastomeric lenses with initially smooth surfaces, the proposed methodology is general and does not rely on any approximation, such as paraxial approximation or thin lens approximation. Therefore, it can be extended to design thin and thick unconventional lenses with irregular shapes as well as surface features (such as cuts, local bulges, or wrinkles) purposefully introduced to further alter the optical response. In parallel, it also enables investigation of different deformation protocols, such as twisting, shearing, and extension followed by bending which has been showed to result in aberration reduction in thin lenses [28,36,37]. Further, generalizations can be achieved by exploring the effect of different materials. For example, by incorporating a temperature dependent viscoelastic model for glass [38–40], one could investigate the effect of deformation applied in the melted state on lenses made of glass, providing new routes for the realization of aberration-free lenses. Finally, while here we have considered spherical aberration, the effect of deformation on different other optical properties, including tilt, coma, and distortion, remains to be explored.

---

[*]bertoldi@seas.harvard.edu
[†]A. Z. and E. M. contributed equally to this work.

[1] E. Siéfert, E. Reyssat, J. Bico, and B. Roman, Bio-inspired pneumatic shape-morphing elastomers, Nat. Mater. **18**, 24 (2019).

[2] E. Siéfert, E. Reyssat, J. Bico, and B. Roman, Programming stiff inflatable shells from planar patterned fabrics, Soft Matter **16**, 7898 (2020).

[3] B. Florijn, C. Coulais, and M. van Hecke, Programmable Mechanical Metamaterials, Phys. Rev. Lett. **113**, 175503 (2014).

[4] K. Bertoldi, V. Vitelli, J. Christensen, and M. Van Hecke, Flexible mechanical metamaterials, Nat. Rev. Mater. **2**, 17066 (2017).

[5] T. Xu, J. Zhang, M. Salehizadeh, O. Onaizah, and E. Diller, Millimeter-scale flexible robots with programmable three-dimensional magnetization and motions, Sci. Rob. **4**, eaav4494 (2019).

[6] A. Miriyev, K. Stack, and H. Lipson, Soft material for soft actuators, Nat. Commun. **8**, 596 (2017).

[7] S. I. Rich, R. J. Wood, and C. Majidi, Untethered soft robotics, Nat. Electron. **1**, 102 (2018).

[8] W. Hu, G. Zhan Lum, M. Mastrangeli, and M. Sitti, Small-scale soft-bodied robot with multimodal locomotion, Nature (London) **554**, 81 (2018).

[9] B. Shin, J. Ha, M. Lee, K. Park, G. Ho Park, T. Hyun Choi, K.-J. Cho, and H.-Y. Kim, Hygrobot: A self-locomotive ratcheted actuator powered by environmental humidity, Sci. Rob. **3**, eaar2629 (2018).

[10] S. Palagi and P. Fischer, Bioinspired microrobots, Nat. Rev. Mater. **3**, 113 (2018).

[11] S. Palagi, A. G. Mark, S. Yik Reigh, K. Melde, T. Qiu, H. Zeng, C. Parmeggiani, D. Martella, A. Sanchez-Castillo, N. Kapernaum *et al.*, Structured light enables biomimetic swimming and versatile locomotion of photoresponsive soft microrobots, Nat. Mater. **15**, 647 (2016).

[12] T. Courtney, M. S. Sacks, J. Stankus, J. Guan, and W. R. Wagner, Design and analysis of tissue engineering scaffolds that mimic soft tissue mechanical anisotropy, Biomaterials **27**, 3631 (2006).

[13] R. Landers, A. Pfister, U. Hübner, H. John, R. Schmelzeisen, and R. Mülhaupt, Fabrication of soft tissue engineering scaffolds by means of rapid prototyping techniques, J. Mater. Sci. **37**, 3107 (2002).

[14] D. P. Holmes and A. J. Crosby, Snapping surfaces, Adv. Mater. **19**, 3589 (2007).

[15] G. C. Knollman, J. L. S. Bellin, and J. L. Weaver, Variable-focus liquid-filled hydroacoustic lens, J. Acoust. Soc. Am. **49**, 253 (1971).

[16] H. Ren and S.-T. Wu, Variable-focus liquid lens, Opt. Express **15**, 5931 (2007).

[17] W. V. De Luca , Variable power fluid lens, U.S. Patent No. 3,161,718 (1964).

[18] S. Shian, R. M. Diebold, and D. R. Clarke, Tunable lenses using transparent dielectric elastomer actuators, Opt. Express **21**, 8669 (2013).

[19] F. Carpi, G. Frediani, S. Turco, and D. De Rossi, Bioinspired tunable lens with muscle-like electroactive elastomers, Adv. Funct. Mater. **21**, 4152 (2011).

[20] K. Hoshino and I. Shimoyama, Analysis of elastic micro optical components under large deformation, J. Micromech. Microeng. **13**, 149 (2002).

[21] S. Schuhladen, S. Petsch, P. Liebetraut, P. Müller, and H. Zappe, Miniaturized tunable imaging system inspired by the human eye, Opt. Lett. **38**, 3991 (2013).

[22] J.-M. Choi, H.-M. Son, and Y.-J. Lee, Biomimetic variable-focus lens system controlled by winding-type sma actuator, Opt. Express **17**, 8152 (2009).

[23] P. Liebetraut, S. Petsch, W. Mönch, and H. Zappe, Tunable solid-body elastomer lenses with electromagnetic actuation, Appl. Opt. **50**, 3268 (2011).

[24] L. Maffli, S. Rosset, M. Ghilardi, F. Carpi, and H. Shea, Ultrafast all-polymer electrically tunable silicone lenses, Adv. Funct. Mater. **25**, 1656 (2015).

[25] A. She, S. Zhang, S. Shian, D. R. Clarke, and F. Capasso, Adaptive metalenses with simultaneous electrical control of focal length, astigmatism, and shift, Sci. Adv. **4**, eaap9957 (2018).

[26] M. Ghilardi, H. Boys, P. Török, J. J. C. Busfield, and F. Carpi, Smart lenses with electrically tuneable astigmatism, Sci. Rep. **9**, 16127 (2019).

[27] P. Liebetraut, S. Petsch, J. Liebeskind, and H. Zappe, Elastomeric lenses with tunable astigmatism, Light Sci. Appl. **2**, e98 (2013).

[28] G. René Lemaitre, *Astronomical Optics and Elasticity Theory: Active Optics Methods* (Springer Science & Business Media, New York, 2008).

[29] F. Rathgeber, D. A. Ham, L. Mitchell, M. Lange, F. Luporini, A. T. T. McRae, G.-T. Bercea, G. R. Markall, and P. H. J. Kelly, Firedrake: Automating the finite element method by composing abstractions, ACM Trans. Math. Softw. **43**, 24:1 (2016).

[30] R. Karl Luneburg, *Mathematical Theory of Optics* (University of California Press, Berkeley, CA, 1966).

[31] E. George Coker and L. N. George Filon, *A Treatise on Photo-elasticity* (Cambridge University Press, Cambridge, England, 1931).

[32] Note that the aberration measure $\mathcal{L}$ used here is closely related to the wavefront aberration measurement defined by the Zernike polynomials (i.e., spherical polynomial coefficient or Z_4^0) [33].

[33] M. Born and E. Wolf, *Principles of Optics: Electromagnetic Theory of Propagation, Interference and Diffraction of Light* (Elsevier, New York, 2013).

[34] See Supplemental Material at http://link.aps.org/supplemental/10.1103/PhysRevLett.126.084301 for finite element model, additional numerical results, analytical reduced order model, and fabrication methods.

[35] We fix one of the two profiles since the surface profile of a lens with zero aberration obtained by equating Eqs. (2) and (4) is not unique [R. G. González-Acuña and J. C. Gutiérrez-Vega, General formula for aspheric collimator lens design free of spherical aberration, in *Current Developments in Lens Design and Optical Engineering XX* (International Society for Optics and Photonics, 2019), Vol. 11104, pp. 111040P].

[36] G. R Lemaitre, Optical design and active optics methods in astronomy, Opt. Rev. **20**, 103 (2013).

[37] P. Zhao, Ç. Ataman, and H. Zappe, Spherical aberration free liquid-filled tunable lens with variable thickness membrane, Opt. Express **23**, 21264 (2015).

[38] M. Arai, Y. Kato, and T. Kodera, Characterization of the thermo-viscoelastic property of glass and numerical simulation of the press molding of glass lens, Journal of Thermal Stresses **32**, 1235 (2009).

[39] A. Jain and A. Y. Yi, Numerical modeling of viscoelastic stress relaxation during glass lens forming process, J. Am. Ceram. Soc. **88**, 530 (2005).

[40] A. Y. Yi and A. Jain, Compression molding of aspherical glass lenses—A combined experimental and numerical analysis, J. Am. Ceram. Soc. **88**, 579 (2005).

[41] Hyperelastic lens aberration (hela), GitHub repository, https://github.com/ahmadzareei/HELA (2020).

S1.   NUMERICAL ANALYSES

In this Section, we first provide details for the Finite Element analyses used to investigate the large deformation of our soft lenses and then describe the geometrical ray tracing simulation conducted to explore the effect of the applied deformation on their optical properties.

A.   Finite Element analyses

In this study we use non-linear Finite Element analyses to determine the configuration of the elastomeric lenses as a function of the applied deformation. In order to numerically solve the problem, we mesh the two dimensional models with a triangular mesh within `gmsh` library, then use higher order boundary conforming elements in `Firedrake` and ascertain the accuracy of each mesh through a mesh refinement study. In our simulations the deformation is applied by prescribing the displacement of the non-refractive boundaries. Further, we capture the response of the elastomers out of which the lenses are made using an almost incompressible neo-Hookean model with strain energy density

$$\psi = \frac{\mu}{2}(\text{tr}(\mathbf{C}) - 3) - \mu \det(\mathbf{F}) + \frac{\lambda}{2}\log(\det \mathbf{F})^2 \tag{S1}$$

where $\mathbf{C} = \mathbf{F}^\top \mathbf{F}$ is the Green-Cauchy strain tensor, $\mathbf{F}$ is the deformation gradient and μ and λ are the Lamé coefficients, which can be written in terms of the Young's modulus, E, and Poisson's ratio, ν as $\mu = E/2(1+\nu)$ and $\lambda = E\nu/(1+\nu)(1-2\nu)$. Note that in the limit of a fully incompressible material our strain energy has the form of

$$\psi = \frac{\mu}{2}(\text{tr}(\mathbf{C}) - 3); \tag{S2}$$

with

$$\det \mathbf{F} = 1. \tag{S3}$$

We then carry out non-linear Finite Element analyses using open-source `Firedrake` library. In our analyses with comressible materials we find the kinematically admissible displacement field $\mathbf{u}$ that minimizes the free-energy

$$\Pi(\mathbf{u}) = \int_\Omega \psi(\mathbf{u}) d\mathbf{x}. \tag{S4}$$

Differently, in the incompressible limit we find the kinematically admissible displacement field $\mathbf{u}$ that minimizes the free-energy

$$\Pi(\mathbf{u}) = \int_\Omega \psi(\mathbf{u}) d\mathbf{x} + \int_\Omega p(\det \mathbf{F} - 1) d\mathbf{x}, \tag{S5}$$

where p is a Lagrange multiplier.   The minimization problem solved using Newton's method. Please refer to the codes available online [1] for more details.

---

* bertoldi@seas.harvard.edu

B.   Geometrical ray tracing

After we obtain the surface profile of the lens using FE simulations, we use geometrical ray tracing to characterize the optical response of lens. For each given deformed configuration, we compute the trajectories of incidents rays that travel parallel to the optical axis. For each ray we find the intersection between the ray and the left surface of the lens (note that we pass a spline through the points on the left surface of the lens to obtain a smoother profile). At the intersection, we then calculate the normal direction to the surface and find the input angle of the ray entering the lens (identified by the angle ϕ in Fig. S1). Next, we use Snell's law to calculate the angle α between the normal to the left surface and the in-lens ray path

$$n_0 \sin \phi = n \sin \alpha, \tag{S6}$$

where n and n_0 denote the refractive index of the lens and surrounding medium. Once α is known, we calculate the angle between the ray and the normal to the right surface, β. Finally, we use Snell's law again to determine the trajectory of the ray after it exits the lens by solving

$$n \sin \beta = n_0 \sin \gamma, \tag{S7}$$

where γ is the angle between normal to the right surface and the ray trajectory outside the lens.
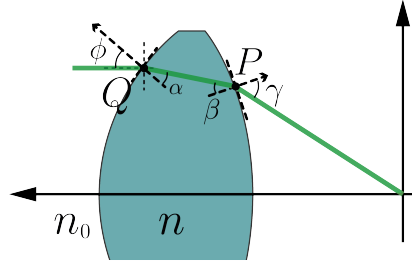   Please refer to the codes available online [1] for more details.

FIG. S1. Schematic of a ray trajectory.
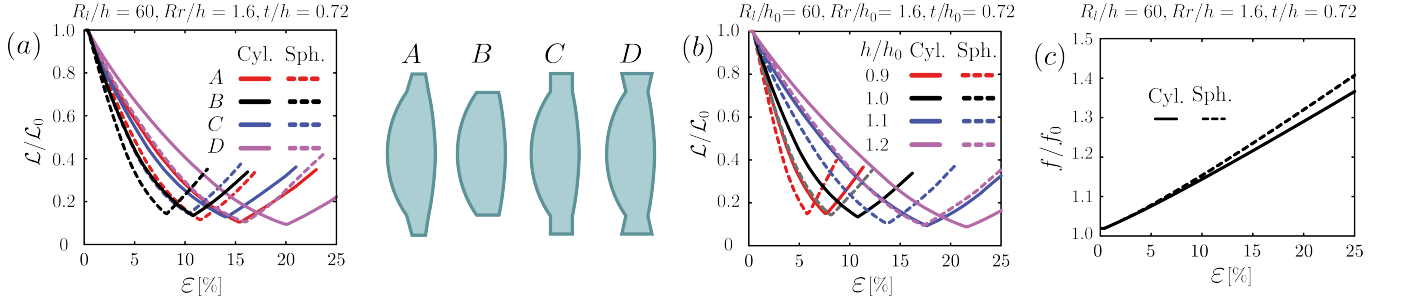
S2. ADDITIONAL NUMERICAL RESULTS

FIG. S2. (a) Effect of boundary conditions on $\mathcal{L}$. Clamped lenses with different end geometries are considered (shown on the right). (b) Effect of h on $\mathcal{L}$ ($h_0 = 25$mm). (c) Focal length variation for a spherical and cylindrical lens as a function of the applied strain.
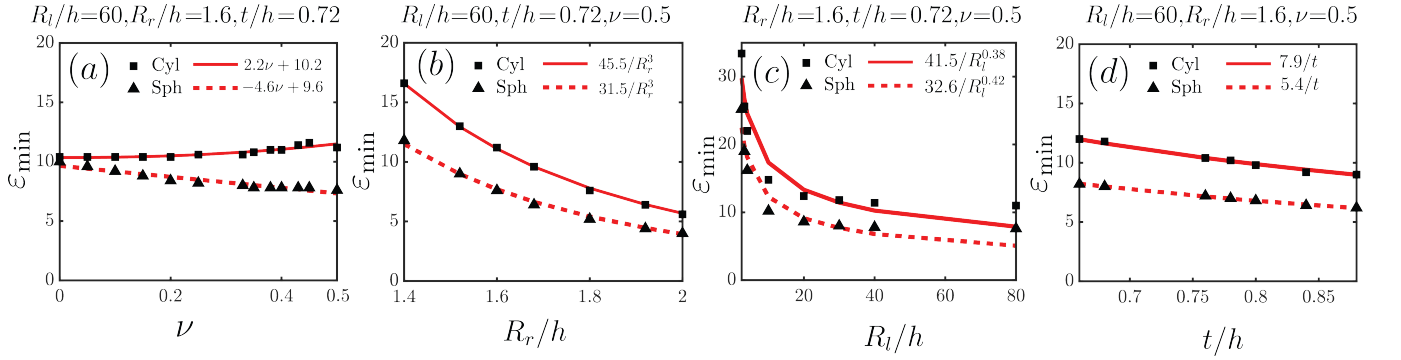

FIG. S3. (a) Evolution of L^2-norm difference between the left surface coordinates of the aberration-free lens and the simulated one, $||x_Q^{An} - x_Q^{FE}||$ (left vertical axis), and aberration, $\mathcal{L}/\mathcal{L}_0$ (right vertical axis), as a function of the applied strain, ε, for a cylindrical and spherical lens characterized by $R_r/h = 60$, $R_l/h = 1.6$ and $t/h = 0.72$. There is a good agreement between the two curves and the minimum values of smallest distance between the surfaces and the lowest value of aberration. Note that the minima of the two curves are slightly offset. Such difference can be attributed to the fact that different metrics are used. The difference between the coordinates is obtained through L^2-norm, while the reduction in aberration is obtained through L$^\infty$-norm. (b)-(c) Difference between the aberration-free and stretched profiles, $x_Q^{An} - x_Q^{FE}$, along the lens height, y/h, for a cylindrical and spherical lens characterized by $R_r/h = 60$, $R_l/h = 1.6$ and $t/h = 0.72$ subjected to (b) stretching and (c) compression.
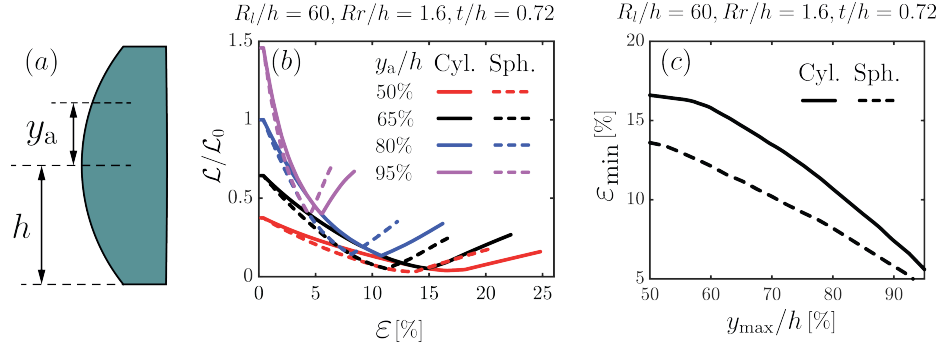
FIG. S4. (a) Schematic of a biconvex lens highlighting the lens height h and the aperture size, y_a. In our analyses the aberration is calculated by considering only far-field rays that enter the left lens surface at points with y-coordinates smaller than y_a. Note that in the main text we consider $y_a = 0.8h$. (b) Effect of lens' aperture y_a/h on aberration $\mathcal{L}/\mathcal{L}_0$ for a cylindrical and spherical lens with $R_r/h = 60$, $R_l/h = 1.6$ and $t/h = 0.72$ subjected to stretching. Note that $\mathcal{L}_0 = \mathcal{L}(\varepsilon = 0)$ for a lens with 80% aperture (i.e. $y_a/h = 80\%$). (c) Evolution of the strain at which the minimum aberration, $\varepsilon_{\min}$, is obtained as a function of the lens' aperture, y_a/h. We find that $\varepsilon_{\min}$ monotonically decreases as y_a/h increases. Note that a smaller aperture results in smaller initial aberration. However, since the central region of the lens is slower in approaching the zero aberration profile, the strain at which the aberration is minimum, $\varepsilon_{\min}$, becomes larger.
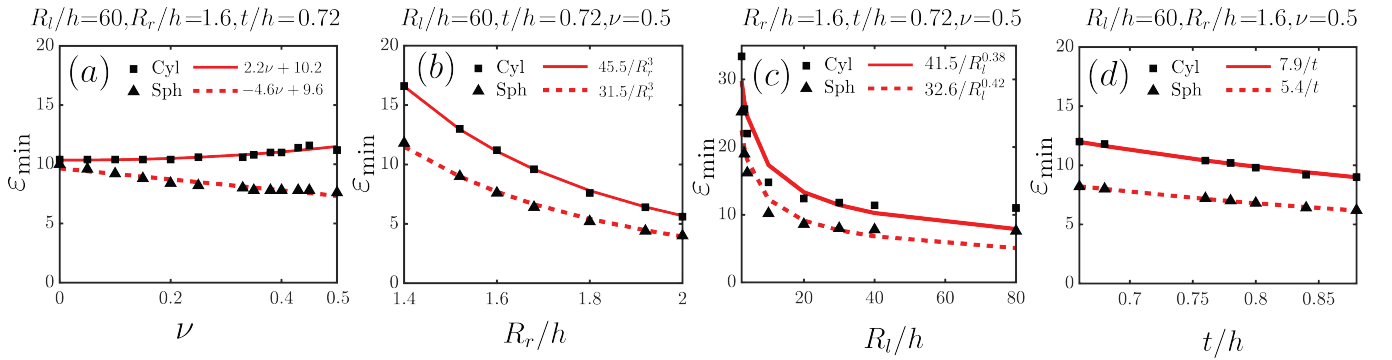

FIG. S5. Effect of material (a) ν, and geometrical parameters (b) R_r, (c) R_l, and (d) t/h on the strain at which the minimum aberration is obtained, $\varepsilon_{\min}$, for both cylindrical and spherical lenses. The markers denote the values of $\varepsilon_{\min}$ extracted from the numerical curves reported in Fig. 4 in the main text. The dash red lines show best numerical fit (power-law or linear) to the data points. Relevant geometric and material properties are reported at the top of each plot.
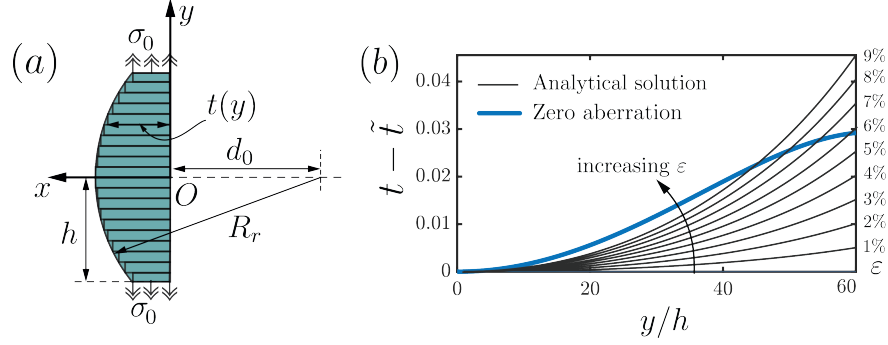
S3. REDUCED-ORDER MODEL

FIG. S6. (a) Schematic of a cylindrical plano-convex lens with the x-axis aligned with the optical axis, and z-axis pointing out of plane, (b) Difference between the initial cylindrical profile and the stretched lens profile, $\tilde{t} - t$, obtained using our reduced model for differnt values of applied strain, ε. The blue line corresponds to the difference between the initial cylindrical surface and the surface with zero aberration.

Our FE analyses indicate that the deformation experienced by a cylindrical lens upon stretching is such that at a critical strain the lens surface approaches the profile of a perfect zero-aberration (so that at this critical strain aberration is largely reduced). Importantly, we find that also a reduced-order model, in which we assume that the right surface remains flat, predicts variation of both deformation and aberration consistent with the numerical simulations. More specifically, in our model we consider a cylindrical lens as a series of infinitesimal hyperelastic rectangular elements undergoing uniaxial deformations and find that the applied stretching introduces an aspherical strain dependent correction to the spherical lens profile.

To facilitate the analysis we use an incompressible Neo-hookean material, whose strain energy density function is given by

$$\psi = \frac{\mu}{2}(\lambda_x^2 + \lambda_y^2 + \lambda_z^2 - 3), \tag{S8}$$

where μ is the shear modulus and λ_x, λ_y, λ_z are the principal stretches, which satisfy the incompressibility constraint

$$\lambda_x \lambda_y \lambda_z = 1. \tag{S9}$$

We will further restrict our analysis to plain-strain conditions, assume $\lambda_z = 1$ and define

$$\lambda \equiv \lambda_y = \frac{1}{\lambda_x}. \tag{S10}$$

Next, we consider a cylindrical lens as a series of infinitesimal hyperelastic rectangular elements and assume that in each element $\sigma_{xx} = 0$. Thus the only non-vanishing component of the Cauchy stress in each infinitesimal element is σ_{yy}, which is given by

$$\sigma_{yy} = \frac{1}{\lambda_x \lambda_z} \frac{\partial \psi}{\partial \lambda_y} = \lambda \frac{\partial \psi}{\partial \lambda} = \mu \left(\lambda^2 - \frac{1}{\lambda^2} \right), \tag{S11}$$

which is homogeneous in each element. Because of traction continuity σ_{yy} can also be obtained as

$$\sigma_{yy}(\tilde{y}) = \frac{F_0}{\tilde{t}(\tilde{y})}, \tag{S12}$$

where F_0 is the total force exerted on the top/bottom boundary, $\tilde{y} = y/\lambda$, and $\tilde{t}(\tilde{y})$ is the deformed cross-sectional thickness of the lens at $\tilde{y}$, which is related to the undeformed cross sectional thickness, $t(y)$, as

$$\tilde{t}(\tilde{y}) = t\left(\frac{y}{\lambda_y}\right) \lambda_x = t\left(\frac{y}{\lambda}\right) \frac{1}{\lambda}. \tag{S13}$$

By using Eqs. (S11), (S12) and (S13) we find that

$$t\left(\frac{y}{\lambda}\right)\left(\lambda - \frac{1}{\lambda^3}\right) = \frac{F_0}{\mu}. \tag{S14}$$

Note that, since the cylindrical lens considered here has one flat side at $x = 0$ and one circular sector with radius R_r and center at $(x_c, y_c){=}(d_0, 0)$ (see Fig. S6a), its thickness is given by

$$t(y) = \sqrt{R_r^2 - y^2} - d_0 \tag{S15}$$

Substitution of Eq. (S15) into Eq. (S14) yields

$$\left(\sqrt{1 - \left(\frac{y}{\lambda R_r}\right)^2} - \frac{d_0}{R_r}\right)\left(\lambda - \frac{1}{\lambda^3}\right) = \frac{F_0}{\mu R_r} \tag{S16}$$

which can be solved to obtain the local stretch λ as a function of height y and applied force F_0. Further, in the limit of small deformations, the principal stretch λ can be expanded around the undeformed configuration as

$$\lambda = 1 + \epsilon + \mathcal{O}(\epsilon^2), \tag{S17}$$

where ϵ denotes the local strain, which is related to the macroscopic engineering strain through

$$\varepsilon = \frac{\int_0^h \epsilon \, dy}{h} = \frac{F_0}{4\mu R_r}\int_0^h \frac{1}{\sqrt{1 - (y/R_r)^2} - d_0/R_r}dy. \tag{S18}$$

By substituting Eq. (S17) into Eq. (S16) and keeping terms up to order $\mathcal{O}(\epsilon^2)$ we obtain

$$\epsilon = \frac{F_0}{4\mu R_r}\frac{1}{\sqrt{1 - (y/R_r)^2} - d_0/R_r}. \tag{S19}$$

Next, we substitute Eqs. (S15), (S17) and and (S19) into Eq. (S13) to express the thickness of the deformed lens as a function of the macroscopic engineering strain as

$$\frac{\tilde{t}(\tilde{y})}{R_r} = f(y) - \left[f(y) + \frac{2(y/R_r)^2}{\sqrt{1 - (y/R_r)^2}}\right]\frac{1/f(y)}{\int_0^h 1/f(y)dy}\varepsilon, \tag{S20}$$

where

$$f(y) = \sqrt{1 - (y/R_r)^2} - \frac{d_0}{R_r} \tag{S21}$$

Importantly, Eq. (S20) defines the left surface profile of the lens, since we assume that the right surface remains flat. In Fig. S6b, we plot the difference between the cylindrical lens profile and the deformed lens profile, $t(y) - \tilde{t}(y)$, for different values of macroscopic strain ε. Further, we show the difference between the cylindrical lens profile and a perfect lens profile with zero-aberration (blue line). In full agreement with the results of our FE simulations, we find that the left surface of the lens approaches the profile of a zero aberration lens as ε increases, but never exactly matches with it.

S4. FABRICATION

To fabricate the cylindrical lens presented in Fig. 1c of the main text we used a molding approach (Fig.S7a). First, a negative mold was fabricated using a 3D printer (Ultimaker3) with Ultimaker PLA material. Then, the lens was cast using a silicone rubber (Slygard 184 Silicone with initial Young's modulus $E = 2.15$ MPa and refractive index $n = 1.4$). Before replication, plastic shims with 0.127 mm thickness were arranged on the surface of the mold corresponding to the refractive surface of the lens to minimize roughness (Fig. S7b). The casted mixture was placed it into the vacuum chamber for about 10 minutes. After the 10 minutes, a large amount of air bubbles appeared on the surface, which were then eliminated by quickly releasing the vacuum chamber valve. Next, to eliminate the remaining bubbles we blew air on the surface of the sample. Note that the process (vacuum-depressurization-blown air) was repeated until all bubbles disappeared. Finally, we let the sample to cure for 2 hours.
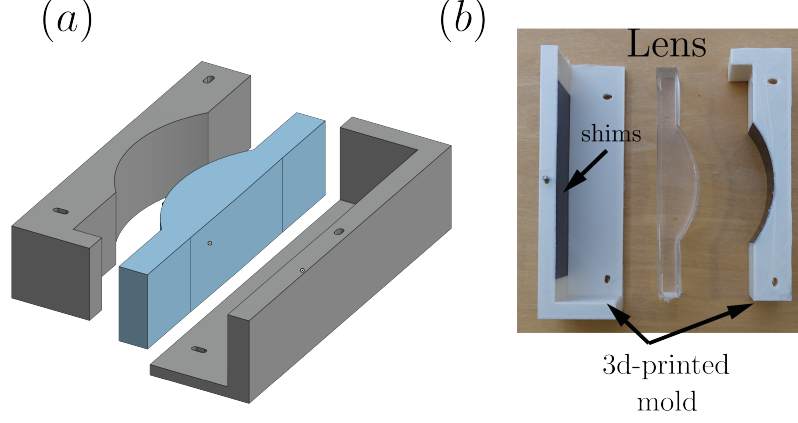
(a) (b)

FIG. S7. Schematic of a bi-convex lens. The coordinate system origin is assumed at the focal point of the lens, and the z-axis is along the optical axis of the lens. The rays parallel to the optical axis enter convex surface at point Q, gets refracted toward the right convex surface and gets refracted at point P toward the focal point at origin.

S5. TESTING

To experimentally characterize both the effect of mechanical deformation on aberration, we clamp the extended boundaries at the two ends of the cylindrical lens with two 3d printed plates securely fastened with two screws and used a linear stage (LTS300mm - Thorlabs) to move one, while keeping the other fixed. In our test we displace the top end of the lens to achieve an apply strain $\Delta\varepsilon = 2\%$ and then use a laser (LT-301 500mW) to characterize the optical response of the lens. Specifically, we point the laser parallel to the optical axis of the lens, slowly move the laser across the deformed lens with another linear stage (LTS150mm - Thorlabs) and record the ray trajectories with a camera (SonyRx400). After the measurements for a given level of applied deformation is complete, we then stretch the lens by 1mm and repeat the measurement. Finally, we use an open library image analysing tools (OpenCV) to extract f and $\mathcal{L}$ from the recorded data.
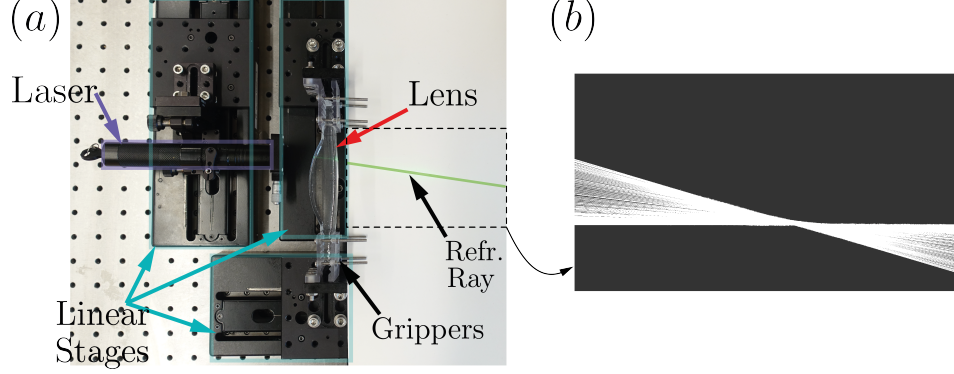

FIG. S8. (a) Experimental setup. (b) Overlayed images of recorded ray trajectories at a given level of deformation.

[1] Hyperelastic lens aberration (hela), `https://github.com/ahmadzareei/HELA` (2020).